Journal for ImmunoTherapy of Cancer

Artificial intelligence-powered spatial analysis of tumor microenvironment in patients with non-small cell lung cancer with acquired resistance to EGFR tyrosine kinase inhibitor

Yeong Hak Bang ,[1,2,3] Geun-Ho Park,[1,4] Jin Woo Oh ,[5] Soohyun Hwang,[5,6] Jun-Gi Jeong,[1,2] Boram Lee,[6] Cheol Yong Joe,[1,4] Hyemin Kim,[1] Jinyong Kim,[1] Sehhoon Park ,[1,4] Hyun Ae Jung,[1] Jong-Mu Sun ,[1] Jin Seok Ahn,[1] Myung-Ju Ahn,[1] Yoon-La Choi,[2,4,6,7] Chang Ho Ahn,[5] Siraj M. Ali,[5] Chan-Young Ock,[5] Se-Hoon Lee[1,2,4]

To cite: Bang YH, Park G-H, Oh JW, *et al*. Artificial intelligence-powered spatial analysis of tumor microenvironment in patients with non-small cell lung cancer with acquired resistance to EGFR tyrosine kinase inhibitor. *Journal for ImmunoTherapy of Cancer* 2025;**13**:e012374. doi:10.1136/jitc-2025-012374

► Additional supplemental material is published online only. To view, please visit the journal online (https://doi.org/10.1136/jitc-2025-012374).

YHB, G-HP and JWO contributed equally.

Accepted 30 September 2025

For numbered affiliations see end of article.

Correspondence to
Dr Se-Hoon Lee;
sehoon.lee119@gmail.com

ABSTRACT

Purpose This study evaluated the dynamic changes in the tumor microenvironment (TME) in patients with non-small cell lung cancer (NSCLC) and acquired resistance to epidermal growth factor receptor (EGFR)-tyrosine kinase inhibitors (TKIs) using an artificial intelligence (AI)-powered spatial TME analyzer. We then assessed the predictive efficacy of immune-checkpoint inhibitors (ICIs)-based treatment.

Experimental design An AI-powered whole-slide image analyzer was used to segment cancer areas (CAs) and cancer stroma and to identify tumor-infiltrating lymphocytes (TILs), tertiary lymphoid structures, fibroblasts, and endothelial cells (ECs) in the tumor tissue. We analyzed 143 NSCLC samples after resistance to EGFR-TKIs from two cohorts: (1) 89 patients treated with ICI monotherapy and (2) 54 patients from the ATTLAS phase III trial comparing atezolizumab plus bevacizumab, paclitaxel, and carboplatin (ABCP) versus pemetrexed plus carboplatin.

Results Post-TKI samples showed reduced TILs in the CA (p=0.045) and increased ECs in the CA (p=0.005) compared with pre-TKI samples. These changes differed according to EGFR mutation subtype. Higher TILs in CA were associated with a better overall response rate (ORR) and progression-free survival (PFS). Similarly, higher EC levels in CA correlated with improved ORR and PFS. In the ATTLAS cohort, these factors were associated with clinical benefits from ABCP, with a significant association with TILs and a marginal association with ECs.

Conclusion Our findings suggest that EGFR-TKIs affect the immune landscape of patients with EGFR-mutated NSCLC. Higher TILs or ECs in the CA were significantly associated with a favorable response to subsequent ICI-based treatment.

Trial registration number NCT03991403.

WHAT IS ALREADY KNOWN ON THIS TOPIC

⇒ Epidermal growth factor receptor (EGFR)-mutant non-small cell lung cancer (NSCLC) is generally unresponsive to immune-checkpoint inhibitors due to an immune-cold tumor microenvironment (TME).

⇒ While EGFR-tyrosine kinase inhibitor (TKI) resistance may induce TME changes, spatial remodeling and its impact on ICI efficacy remain unclear.

⇒ Artificial intelligence (AI)-based spatial analysis has shown potential in predicting immunotherapy outcomes but has not been applied in this setting.

WHAT THIS STUDY ADDS

⇒ Using an AI-powered spatial analyzer, this study assessed paired pre-TKI and post-TKI samples from patients with EGFR-mutant NSCLC.

⇒ Post-TKI samples exhibited decreased intratumoral tumor-infiltrating lymphocytes (TILs) and increased endothelial cells (ECs), with distinct patterns based on EGFR mutation subtype.

⇒ Higher TIL or EC levels after TKI resistance were associated with better response and progression-free survival to ICI-based therapies.

⇒ AI-derived features correlated well with transcriptomic data, supporting their biological and clinical relevance.

HOW THIS STUDY MIGHT AFFECT RESEARCH, PRACTICE OR POLICY

⇒ This approach enables non-invasive, scalable TME profiling from H&E slides.

⇒ Spatial biomarkers may guide immunotherapy decisions in EGFR-TKI-resistant NSCLC.

⇒ Incorporating EC metrics may enhance predictive accuracy beyond TILs alone.

INTRODUCTION

Epidermal growth factor receptor (EGFR) mutations represent a major molecular subtype of non-small cell lung cancer (NSCLC), accounting for approximately 40%–60% of cases in South-East Asian

populations and 10%–20% of Caucasians.[1] EGFR tyrosine kinase inhibitors (TKIs)-based treatments serve as the standard first-line treatment for NSCLC harboring *EGFR* mutations, owing to their remarkable efficacy.[2–6] However, nearly all patients eventually develop acquired resistance to TKIs, leaving platinum-based chemotherapy as the standard second-line option, despite its limited benefits. This highlights the urgent need for novel strategies to improve outcomes after the development of resistance to EGFR-TKIs.

Immune checkpoint inhibitors (ICIs) have demonstrated significant survival benefits in patients with NSCLC without driver mutations.[7–9] However, *EGFR*-mutant NSCLC has consistently shown limited responsiveness to ICIs, largely because of the immune-cold tumor microenvironment (TME).[10 11] Moreover, combination therapies of ICIs with platinum-doublet chemotherapy have failed to show statistically significant clinical benefits compared with platinum-doublets alone in this population.[12 13] Despite these challenges, some studies have reported remarkable responses to ICI monotherapy in specific subsets of patients.[14] Additionally, recent phase III randomized clinical trials (ATTLAS) have shown that adding atezolizumab and bevacizumab to chemotherapy improves the median progression-free survival (PFS) compared with chemotherapy alone in patients with EGFR-TKIs resistance.[15] These findings underscore the need for predictive biomarkers to identify patients who are most likely to benefit from ICIs monotherapy or combination treatment with ICIs after developing resistance to EGFR-TKIs.

Emerging evidence suggests that significant changes occur in the TME after resistance to EGFR-TKIs[14] develops, which may affect the efficacy of ICIs. The spatial heterogeneity of tumor-infiltrating lymphocytes (TILs), tertiary lymphoid structures (TLS), cancer-associated fibroblasts (CAFs), as well as angiogenic signals are key factors influencing treatment outcomes.[16–19] However, quantifying the spatial distribution of these TME constituents (ie, their localization within tumor vs stromal areas) is challenging. Additionally, limitations arise in assessing the spatial distribution on H&E whole-slide images (WSIs) owing to interobserver variability.[20 21]

To address these challenges, we previously demonstrated the clinical utility of an artificial intelligence (AI)-powered spatial TIL analyzer (Lunit SCOPE IO, Lunit, Seoul, South Korea) applied to H&E WSIs to classify immune phenotypes (IPs) as inflamed, immune-excluded, or immune-desert based on the spatial distribution of TILs, showing its ability to stratify patients with distinct survival outcomes across multiple cancer types, including NSCLC.[22–24] In addition, AI-based quantification of other TME components—including TLSs, endothelial cells (ECs), and fibroblasts (Fibs)—has also shown promise in identifying novel prognostic and predictive biomarkers.[25–27]

In the present study, we aimed to evaluate four major objectives: first, using our previously published AI-powered IP (AI-IP) analyzer based on TIL spatial distribution, we sought to assess dynamic changes in IPs before and after EGFR-TKI resistance. Second, we aimed to introduce an extended version of our AI-powered TME analyzer that integrates TIL-based classification and spatial features of TLSs, ECs, and Fibs and evaluated its robustness through validation with spatial transcriptomics and bulk RNA sequencing data. Third, we applied an AI-powered TME analyzer to H&E-stained slides from paired pre-TKI and post-TKI tumor samples of patients with EGFR-mutant NSCLC to investigate dynamic changes in the composition and spatial distribution of TME constituents. Fourth, we evaluated the predictive value of post-TKI TME profiles for response to ICI monotherapy or combination therapy using data from a real-world clinical cohort and a post hoc analysis of the ATTLAS randomized trial.[15]

MATERIALS AND METHODS

Patients and materials

Patients' data and pathological slides were collected from Samsung Medical Center. Key eligibility criteria included pathologically confirmed NSCLC and the presence of EGFR mutations identified by molecular testing, radiologic disease progression after EGFR tyrosine kinase inhibitor (TKI) treatment, and subsequent treatment with ICI-based therapy following EGFR-TKI resistance. Patients were excluded if archival tissue or pathological slides obtained after EGFR-TKI treatment were not available.

Immune phenotyping using AI-powered TIL analyzer

We first applied our previously developed AI-IP analyzer,[24 28] which classifies tumors into inflamed, immune-excluded, or immune-desert categories according to the spatial distribution of TILs. The WSIs are divided into tiles of 0.5 mm×0.5 mm each. Tiles classified as having an inflamed IP were defined by an intratumoral TIL (iTIL) density ≥130/mm². The immune-excluded IP was characterized by an iTIL density <130/mm² combined with a stromal TIL (sTIL) density ≥260/mm², whereas the immune-desert IP was assigned when both iTIL and sTIL densities were below these thresholds.

The distribution of phenotypes across the tiles was analyzed to determine the slide-level IP for a specific WSI. A WSI was classified as inflamed IP if ≥33.3% of the tiles exhibited the inflamed IP within the WSI. If ≥33.3% of the tiles showed the immune-excluded IP and the proportion of inflamed IP tiles was <33.3%, the WSI was categorized as immune-excluded IP. In cases where neither of these conditions was met, the WSI was designated as an immune-desert IP.

AI-powered TME analyzer using WSI

To extend beyond TIL-based phenotyping, we further applied an expanded version of the AI-powered TME analyzer. The AI-powered H&E WSI analysis tool, Lunit SCOPE IO (Lunit), was developed using data from >26

tumor types, including NSCLC. The analyzer is based on a multilevel deep learning architecture described by Ryu *et al*.[29] Detailed information for the model is described in online supplemental methods and online supplemental tables 1 and 2.

Validation of AI-powered cell type predictions using spatial transcriptomics

For more objective evaluation, we validated cell type prediction by the AI model, by demonstrating that the AI-predicted cell types exhibit differential gene expression of well-characterized cell type markers. A paired H&E image and Xenium spatial transcriptomic dataset from a lung adenocarcinoma case (https://www.10xgenomics.com/datasets/preview-data-ffpe-human-lung-cancer-with-xenium-multimodal-cell-segmentation-1-standard)[30] was used (a panel of 377 tumor-related and TME-related genes). The Xenium analysis pipeline provided xy cell coordinates with cell-level transcript quantification. We matched Xenium-detected cells with Lunit SCOPE IO-detected cells by identifying the reciprocally nearest pairs based on physical distance, with a median and mean distance of <2 µm.

We identified gene markers for each cell type inferred from the model through differential gene expression analysis. For example, for each of the 377 genes, we calculated the fraction of model-predicted ECs with transcript detection ($N_{transcript}>0$) and compared it against the detection fraction across all other cells. The statistical significance of differential enrichment was assessed using Fisher's exact test. To address the imbalance in cell type populations within the slide, bootstrap sampling was performed by selecting a set of 1000 ECs and another set of 1000 cells from all other classes. The enrichment statistics were computed and averaged across 100 independent bootstrap samples. This analysis was repeated for tumor cells, TILs, and Fibs.

The biological relevance of the identified gene markers in the model-inferred cell types was assessed using bulk RNA sequencing (RNA-seq) data of relevant cells from the Encyclopedia of DNA Elements consortium portal (encodeproject.org).[31] The cell samples included lung microvascular ECs, Calu-3 lung adenocarcinoma cells, activated T-cells, and lung Fibs. We averaged the transcripts per million values from experimental replicates. The gene quantification files used for this analysis were accessed by searching for the following accession IDs in the portal: ENCFF506QCN/ENCFF953GWT (lung ECs), ENCFF472SUX/ENCFF425ABP (lung adenocarcinoma cells), ENCFF952MIY/ENCFF532XCI (lung Fibs), and ENCFF810MOY/ENCFF090JUO (activated T cells; online supplemental figure S1).

Programmed death-ligand 1 immunohistochemistry

Programmed death-ligand 1 (PD-L1) IHC was performed using the PD-L1 IHC 22C3 PharmDx assay and Dako Autostainer Link 48 (Dako, California, USA) according to the manufacturer's instructions. PD-L1 expression was determined using tumor proportion score (TPS).

Bulk RNA sequencing

RNA extraction and sequencing

Tumor tissues obtained from patients with NSCLC were dissected at 20–40 mg and homogenized 3–4 times for 15 s at 30 Hz using a Tissue Lyser II (Qiagen, Hilden, Germany). RNA was extracted using an RNeasy Mini Kit (Qiagen) according to the standard tissue RNA extraction protocol. Total RNA concentration was calculated using Quant-IT RiboGreen (R11490; Invitrogen, Waltham, Massachusetts, USA). To assess the integrity of total RNA, the samples were evaluated using a TapeStation RNA screentape (5067–5576, Agilent, Santa Clara, California, USA). Only high-quality RNA preparations (RNA integrity >7.0) were used for the library construction. Total RNA was subjected to rRNA depletion using a Ribo-Zero Gold rRNA Removal Kit (MRZG12324, Illumina, San Diego, California, USA). Subsequently, 2 µL of a 100-fold diluted external RNA controls consortium (ERCC) Mix2 solution of the ERCC RNA Spike-In Mix (4456740, Ambion, Austin, Texas, USA) was added. An RNA-seq library was prepared using the TruSeq RNA Sample Prep Kit (Illumina). The libraries were then subjected to an Illumina HiSeq2000 platform (Illumina), and paired-end (2×100 bp) sequencing was performed by Macrogen (Seoul, South Korea).

RNA-seq data preprocessing

RNA-seq datasets were processed using the STAR-RSEM workflow executed via the nf-core/RNA-seq pipeline (V.3.14.0) in Nextflow[31] under default parameter settings. All analyses were conducted on an Ubuntu V.18.04.6 operating system, with containerized environments managed through Docker to ensure reproducibility. Raw sequencing reads were trimmed using TrimGalore (V.0.6.5) to remove adapter sequences and low-quality bases. The cleaned reads were aligned with the human reference genome (hg38) using the STAR software (V.2.7.10a). Gene-level quantification was performed using RSEM (V.1.3.1) with reference to the GENCODE V.46 annotation. Following completion of the pipeline, quality-control metrics, including alignment rates, duplication rates, and read distribution across genomic features, were reviewed using MultiQC (V.1.19) and RSeQC (V.5.0.2).

RNA-seq data analysis

Gene-level quantification was normalized using the trimmed mean of M-values method, and low-abundance genes were excluded to improve the robustness of downstream analyses. To account for potential batch effects, the remove batch effect function of the Limma package (V.3.58.1)[32] was applied.

Correlation analysis between RNA-seq data and Luni-derived variables

TME subtype was classified according to the method described by Bagaev *et al*.[16] Single-sample gene set enrichment analysis (ssGSEA) was performed using the GSVA[33] package (V.1.50.5) to calculate the pathway-level activity scores for individual samples. Predefined gene sets were curated from various sources to assess specific biological features. The following gene sets were derived from the Molecular Signatures Database[34]: angiogenesis, vascular endothelial growth factor (VEGF) signaling, antigen presentation, and B-cell receptor signaling. Additional gene sets included interferon-gamma (IFNG),[35] cytolytic activity,[36] immunologic constant of rejection signature,[37] T-cells, B-cells,[38] CAFs,[16] and TLS signatures 1,[19] 2,[39] and 3.[40] Spearman's rank correlation coefficients were calculated to explore the relationship between ssGSEA-derived pathway activity scores and Lunit-derived variables. In addition, the relationship between TME subtypes derived from RNA-seq data using the method described by Bagaev *et al*[16] and Lunit IP types was analyzed.

Statistical analysis

The normality of continuous variables was assessed using the Shapiro-Wilk test. For paired comparisons, appropriate statistical tests were applied based on data distribution. Paired t-tests were used for normally distributed data, whereas Wilcoxon signed-rank tests were used for non-normally distributed data. Categorical variables were compared using the χ^2 test or Fisher's exact test. Overall survival (OS) was defined as the time from the start of antiprogrammed cell death protein 1 (PD-1)/PD-L1 therapy or enrollment in the ATLLAS trial to the date of death from any cause or the last follow-up. PFS was defined as the time from the initiation of anti-PD-1/L1 therapy or enrollment in the ATLLAS trial to the date of disease progression, as determined using RECIST V.1.1. The Kaplan-Meier method was used to estimate survival outcomes, which were compared between groups using the log-rank test. Univariable and multivariable analyses for PFS and OS were performed using Cox proportional hazard models, with variables showing a univariable p value ≤0.1 entered into the multivariable models. Interactions between TME phenotypes and key baseline clinicopathological characteristics were analyzed using a stratified Cox proportional hazards model. Cut-off values for spatial features such as TILs, ECs, TLSs, and Fibs were identified using maximally selected rank statistics implemented in the 'maxstat' R package,[41] based on their association with survival outcomes. These thresholds were then used to stratify patients into high and low groups. A p value of <0.05 was considered statistically significant. All statistical analyses were performed using the R software (V.4.3.2; R Foundation for Statistical Computing, Vienna, Austria).

RESULTS

Patients and study design

We initially screened patients who underwent ICI therapy after acquiring resistance to EGFR-TKIs between October 2015 and July 2022 at the Samsung Medical Center, Seoul, Korea. In addition, we conducted a post hoc analysis of patients in the ATTLAS trial,[15] who had H&E-stained tissue sample slides after acquiring resistance to EGFR-TKI. In total, 157 NSCLC patient samples were available for analysis. Among them, 143 patients were eligible for the current analysis after excluding 14 patient samples that did not meet the tissue quality criteria for the AI-powered WSI analysis. Among these, 89 patients (62.2%) had paired tumor tissue samples prior to treatment with EGFR-TKIs. A total of 89 patients were treated with ICI monotherapy after resistance to EGFR-TKIs developed and 54 patients were enrolled in the ATTLAS clinical trials; 36 patients were treated with atezolizumab plus bevacizumab, paclitaxel, and carboplatin (ABCP); and 18 patients were treated with pemetrexed plus carboplatin (PC) (figure 1A).

Using Lunit SCOPE IO (Lunit), we initially conducted AI-IP analysis,[22–24] classifying pre-TKI and post-TKI samples into inflamed, immune-excluded, or immune-desert phenotypes based on TIL spatial distribution. We then evaluated how EGFR-TKI treatment affected the changes in these IPs and whether these changes could effectively predict prognosis following subsequent ICI-based monotherapy or combination therapy. Furthermore, using an AI-powered TME analyzer, we conducted a detailed comparison of key components, including TILs, TLSs, ECs, and Fibs, to assess the dynamic changes following TKI treatment and their potential roles in predicting the efficacy of ICI-based therapy.

For biological validation, we further analyzed the H&E slides from the public Xenium spatial transcriptomics dataset (10x Genomics, Pleasanton, California, USA) using an AI-powered TME analyzer to compare the distribution and characteristics of ECs, Fibs, TILs, and tumor cells, and validated the findings with spatial transcriptomic data. In addition, we compared the AI-powered TME analyzer inference results with bulk RNA-seq data from 42 samples (10 pre-TKI and 32 post-TKI samples from our cohort).

Landscape of AI-IP analysis

The Lunit SCOPE IO model is an AI-IP analyzer that classifies IP based on spatial TIL distribution and density. To perform spatial analysis of TILs distribution within WSI of various sizes, each WSI was divided into 0.5 mm×0.5 mm tiles, with the IP of each tile classified based on the following criteria: tile-level inflamed IP, if the TIL density within the total cancer area (CA) in the tile is ≥130/mm^2 (in which CA refers to cancer epithelium or, in the case of nonepithelial tumors, the nonstromal tumor cells); tile-level immune-excluded IP, if the TIL density within the total CA is <130/mm^2 and that within the total cancer stroma (CS) is >260/mm^2; and tile-level immune-desert IP, if the TIL densities are below threshold in both the CA and CS within the tile. The overall WSI-level inflamed score, immune-excluded score, and immune-desert scores were calculated by dividing the number of tiles

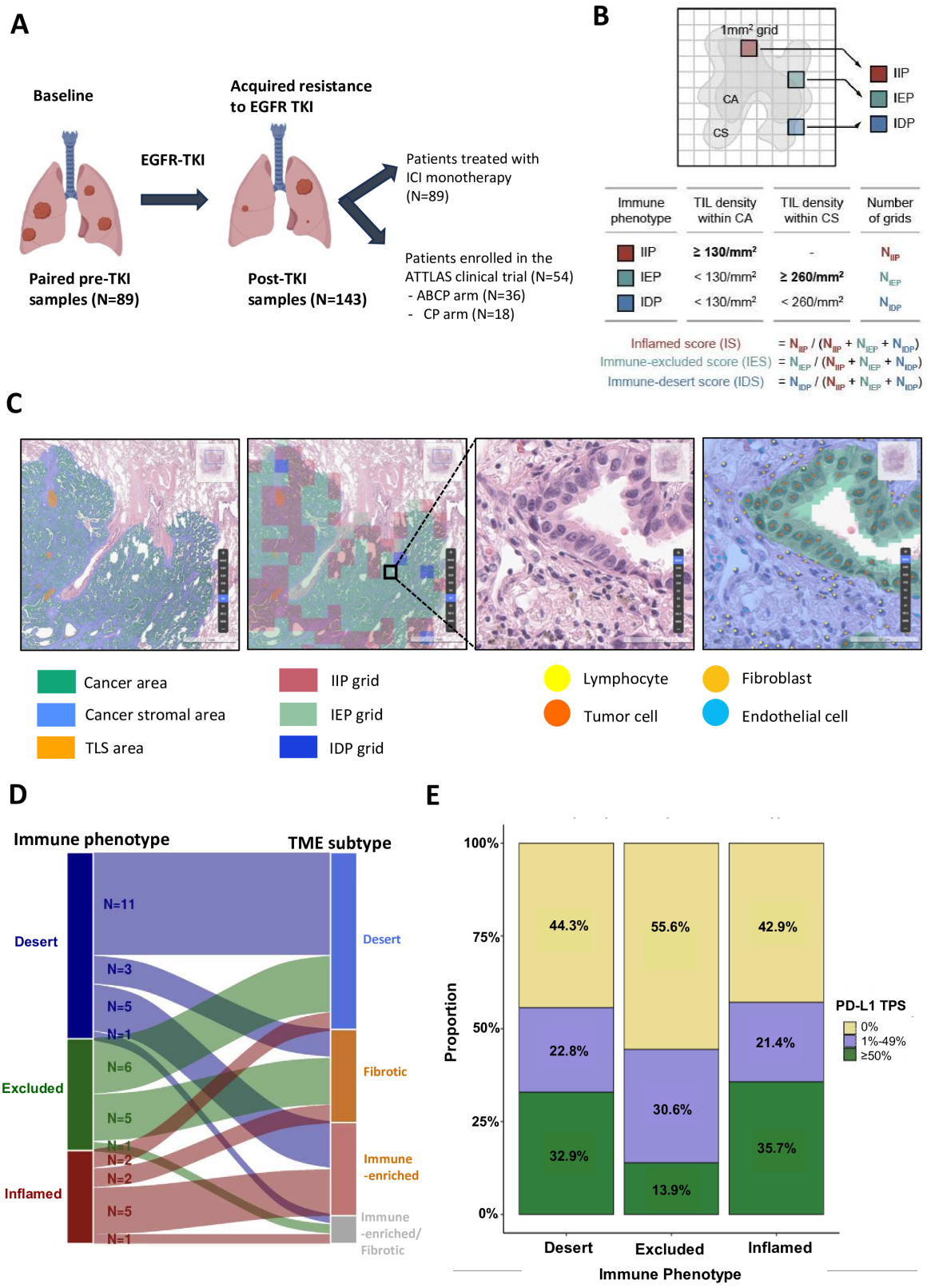

Figure 1 The scheme of AI-powered TME analyzer and the workflow of the current study. (A) Study flow diagram. (B) Landscape of AI-IP analysis. (C) Representative images of TME analyzer. (D) Alluvial plot presenting the comparison of the AI-IP and RNA expression-based TME subtype. (E) Proportional bar plot showing PD-L1 expression tumor proportion scores, according to immune phenotype. ABCP, atezolizumab plus bevacizumab, paclitaxel, and carboplatin; AI, artificial intelligence; AI-IP, artificial intelligence-powered immune-phenotype; CA, cancer area; CP, carboplatin plus paclitaxel; CS, cancer stroma; EGFR, epidermal growth factor receptor; IDP, immune-desert immune phenotype; IEP, immune-excluded immune phenotype; IIP, inflamed immune phenotype; PD-L1, programmed death-ligand 1; TIL, tumor-infiltrating lymphocyte; TKI, tyrosine kinase inhibitor; TME, tumor microenvironment; TPS, tumor proportion score.

with the respective phenotypes by the total number of tiles analyzed (figure 1B). The representative IP for each WSI was as follows: inflamed when the inflamed score was ≥33.3%, immune-excluded when the immune-excluded score was ≥33.3% and the inflamed score was <33.3%, and immune-desert otherwise (figure 1B,C).

We further analyzed RNA-seq results from samples collected pre-TKI and post-TKI to evaluate the robustness of the AI-IP analysis. When comparing previously defined transcriptomic-based TME subtypes,[16] half of the inflamed AI-IP were immune-enriched subtypes (5/10, 50.0%), whereas most of the patients with immune-excluded AI-IP and immune-desert AI-IP were classified as fibrotic or immune-enriched and fibrotic subtypes (6/12, 50.0%) and as depleted subtypes (11/20, 55.0%), respectively (figure 1D). The proportion of patients with PD-L1 TPS ≥50% was not significantly different based on the AI-IP (32.9% vs 13.9% vs 35.7%, p=0.292) (figure 1E).

Validation of AI-based cell type predictions by AI-powered TME analysis using spatial transcriptomics

We validated the WSI-based AI cell-type prediction by quantifying cell-specific gene expression levels in each of the AI-predicted cell types using a paired dataset of H&E WSI and Xenium spatial transcriptomic in lung adenocarcinoma (figure 2A–F). We mapped spatial transcriptomic-detected transcripts (from 377 genes in the Xenium panel of tumors and TME-related genes) to AI-predicted cell coordinates in the WSI (figure 2A,B). Through differential gene expression analysis, we identified canonical marker genes for each AI-predicted cell type: ECs (eg, *VWF* and *PECAM1*),[42 43] TILs (eg, *CD3E*), Fibs (eg, *ACTA2* and *COL5A2*),[44 45] and tumor cells (*EPCAM*; figure 2C–F). In addition, other identified gene markers were also assessed through bulk RNA-seq data of relevant cells from the ENCODE consortium portal (encodeproject.org[31]; online supplemental figure S1).

Correlation between TILs, Fibs, ECs, and TLSs inferred by Lunit SCOPE IO and bulk transcriptomics data

We further conducted a correlation analysis between the AI-powered segmentation results of TILs, TLS, ECs, and Fibs and RNA-seq derived scores in the combined pre-TKI and post-TKI samples (figure 2G–H). TILs on CA were significantly positively correlated with the IFNG signature (ρ=0.498, p<0.001), and ECs on CA with the angiogenesis signature (ρ=0.315, p=0.042), but not VEGF signatures (ρ =0.183, p=0.710). Fibs across CA and CS were associated with the cancer-associated fibroblast signature (ρ=0.581, p<0.001), and TLS area per CA correlated with the TLS signature 3 (ρ =0.439, p=0.003), respectively.

Patient characteristics

Baseline characteristics are summarized in table 1 and online supplemental table 3. The median age of patients treated with ICI or enrolled in the ATLLAS trial was 64 (range 32–93) years. Of the patients, 69 were male (48.3%) and 85 had never smoked (table 1). Among the patients who underwent ICI monotherapy, most patients underwent platinum-based treatment prior to ICIs, and approximately half of the patients underwent ICIs as third-line treatment (n=49, 55.1%; table 1). More than half of the patients (n=55, 61.8%) showed exon 19 deletion (19del) mutation, and 32 patients had L858R mutation (n=32, 55.6%) when they received first-line EGFR-TKI. Approximately half of the patients (n=64, 44.7%) acquired T790M mutation after first-line EGFR-TKI treatment (online supplemental table 3 and figure 3A). The median duration of EGFR-TKI was 12.7 months (range 4.8–71.8 months).

Dynamic changes of the TME after acquired resistance to EGFR-TKI

We compared the TPS of the 32 patients with the available pre-TKI and post-TKI TPS data. The TPS was increased after EGFR-TKI (figure 3B), showing patients with a TPS ≥50% increased from seven (21.9%) to 14 (43.8%) after EGFR-TKI (figure 3C). Among the 89 patients with paired pre-TKI and post-TKI pathological samples, IP of pre-TKI biopsy exhibited inflamed in 10 (11.2%), immune-excluded in 26 (29.2%), and immune-desert in 53 (59.6%). Among the 10 inflamed IP, three patients (30.0%) remained with inflamed IP, two of 26 with immune-excluded IP (7.6%), and eight of 53 with immune-desert IP (15.1%) changed to inflamed IP after EGFR-TKI (figure 3D).

We further compared the TILs on CA, TLS per CA, ECs on CA, and Fibs across CA and CS before and after TKI treatment. Interestingly, while no significant differences were found in TLS per CA (p=0.884) and Fibs on CA (p=0.819), TILs on CA were significantly decreased (p=0.045), whereas ECs on CA were significantly elevated after resistance to EGFR-TKI treatment (p=0.006; figure 3E).

Notably, no significant differences in TILs on CA or ECs on CA were observed among the EGFR mutation subtypes or post-TKI T790M status in the pretreatment samples (online supplemental figure S2A), and the change patterns of the TME varied according to the EGFR mutation subtype and the presence of acquired T790M mutation after EGFR-TKI treatment (figure 4). In patients with the L858R mutation, there was a significant increase in ECs on CA (p=0.009), whereas TILs on CA were generally maintained without a notable reduction (p=0.625). In contrast, patients with 19del (p=0.045) or acquired T790M mutations exhibited a reduction in TILs on CA (p=0.033), whereas no significant difference was observed in ECs on CA (p=0.221 and p=0.097, respectively), compared with others (figure 4). Comparative analysis between post-TKI samples indicated significantly higher ECs (p=0.009) and TILs (p=0.023) in the CA in L858R than in patients with 19del (online supplemental figure S2B). Furthermore, among post-TKI samples, T790M-positive tumors demonstrated significantly lower TILs compared with T790M-negative tumors (p<0.001),

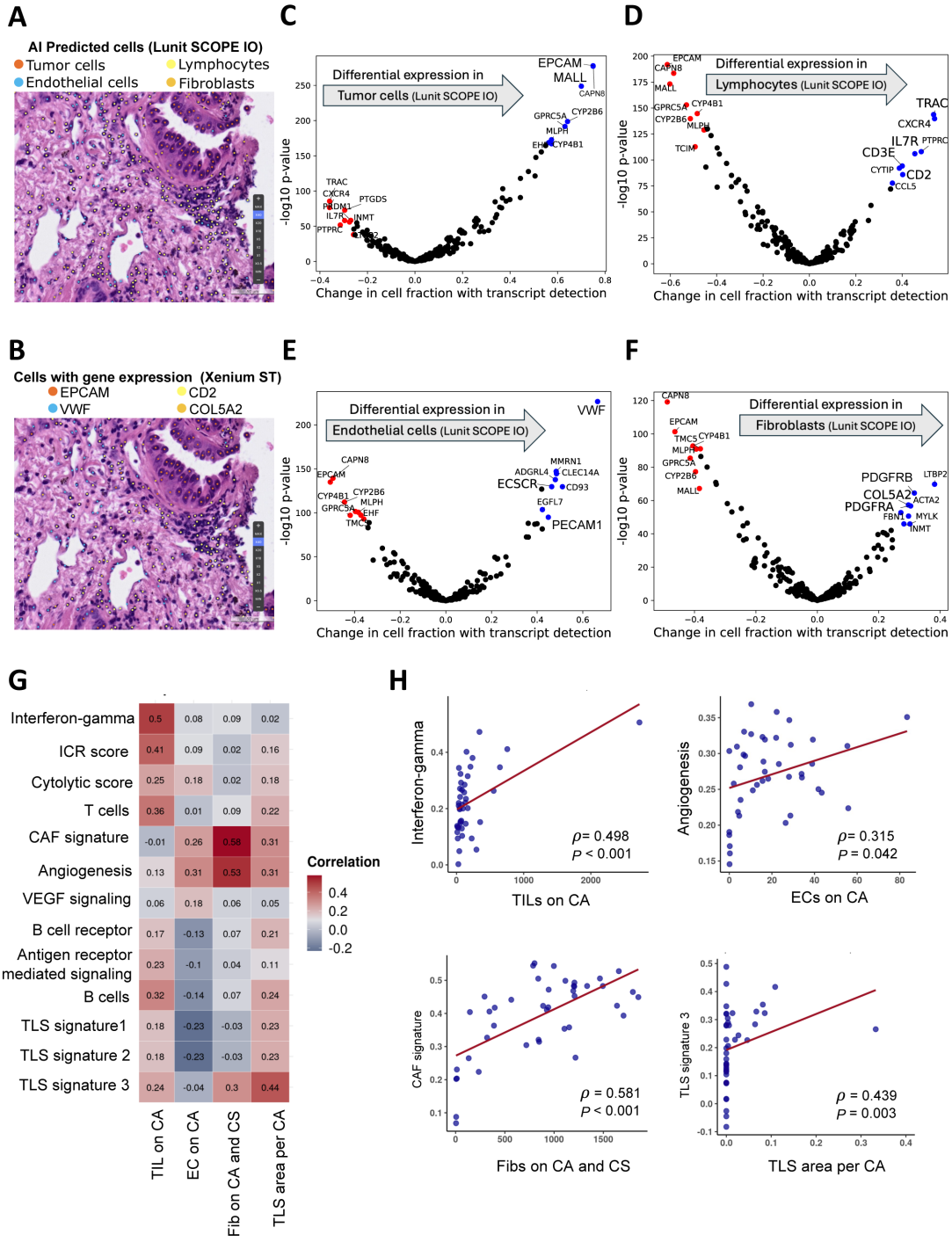

Figure 2 Transcriptomic characteristics of TME assessed by AI-powered spatial analysis. (A–B) Representative figure showing the spatial distribution of AI-powered inferred cells and their matched Xenium points from spatial transcriptomics data. Comparison between cell inference based on an AI-powered TME analyzer (upper panel) and gene expression data from spatial transcriptomics (lower panel; Xenium, 10x Genomics). Spatial transcriptomic data were downloaded from the 10x Genomics website (https://www.10xgenomics.com/datasets/preview-data-ffpe-human-lung-cancer-with-xenium-multimodal-cell-segmentation-1-standard). (C–F) Volcano plots showing DEGs in the spatial transcriptomic data matched with AI-predicted cell types from H&E slides for tumor cells (C), lymphocytes (D), ECs (E), and Fibs (F). A paired H&E image and Xenium spatial transcriptomic dataset from a lung adenocarcinoma case were used, focusing on a panel of 377 tumor-related and TME-related genes. The X-axis represents the change in the cell fraction with transcript detection relative to other cell types. The cell fraction was defined as the fraction of AI-predicted cell types that expressed specific genes. The Y-axis represents the –log10(p value) calculated using Fisher's exact test. (G) Correlation heatmap of the transcriptomics-based score and AI-powered TME analysis. (H) Scatter plots showing the correlation between transcriptomics-based scores and the AI-powered TME. AI, artificial intelligence; CA, cancer area; CAF, cancer-associated fibroblast; CS, cancer stroma; DEG, differentially expressed gene; EC, endothelial cell; Fib, fibroblast; ICR, immunological constant of rejection; TIL, tumor-infiltrating lymphocyte; TME, tumor microenvironment; TLS, tertiary lymphoid structure; VEGF, vascular endothelial growth factor.

Table 1 Baseline characteristics

	Total (n=143)	Patients treated with ICI monotherapy (n=89)	Patients enrolled in the ATTLAS clinical trial (n=54)
Age ≥65 years	57 (39.9%)	33 (37.1%)	24 (44.4%)
Sex			
Male	69 (48.3%)	43 (48.3%)	26 (48.1%)
Female	74 (51.7%)	46 (51.7%)	28 (51.9%)
ECOG			
0	12 (8.4%)	5 (5.6%)	7 (13.0%)
1	126 (88.1%)	79 (88.8%)	47 (87.0%)
2	5 (3.5%)	5 (5.6%)	0 (0.0%)
Smoking history			
Never smoker	85 (59.4%)	54 (60.7%)	31 (57.4%)
Ex-smoker	42 (29.4%)	26 (29.2%)	16 (29.6%)
Current-smoker	16 (11.2%)	9 (10.1%)	7 (13.0%)
EGFR mutation status			
L858R	50 (35.0%)	29 (32.6%)	21 (38.9%)
19del	91 (63.6%)	59 (66.3%)	32 (59.3%)
Others	2 (1.4%)	1 (1.1%)	1 (1.9%)
Acquired T790M mutation			
Positive	64 (44.8%)	34 (38.2%)	30 (55.6%)
Negative	79 (55.2%)	55 (61.8%)	24 (44.4%)
First EGFR-TKI			
Gefitinib	52 (36.4%)	23 (25.8%)	29 (53.7%)
Erlotinib	14 (9.8%)	13 (14.6%)	1 (1.9%)
Afatinib	74 (51.7%)	53 (59.6%)	21 (38.9%)
Osimertinib	1 (0.7%)	0 (0.0%)	1 (1.9%)
Lazertinib	2 (1.4%)	0 (0.0%)	2 (3.7%)
Exposure to platinum prior to ICI		82 (92.1%)	
ICI regimen			
Atezolizumab		48 (53.9%)	
Pembrolizumab		35 (39.3%)	
Nivolumab		5 (5.6%)	
Durvalumab		1 (1.1%)	
ICI treatment line			
2		7 (7.9%)	
3		49 (55.1%)	
≥4		33 (37.1%)	

The data are presented as numbers (%).
19del, exon 19 deletion; ECOG, Eastern Cooperative Oncology Group; EGFR, epidermal growth factor receptor; ICI, immune-checkpoint inhibitor; TKI, tyrosine-kinase inhibitor.

with marginally lower ECs on cancer in T790M-positive tumors (p=0.054) (online supplemental figure S2B).

Efficacy outcomes after acquired resistance for EGFR-TKI according to the AI-powered TME subgroups

With a median follow-up duration of 45.9 months, inflamed IP after TKI showed higher overall response (38.5% vs 9.9%, p=0.006) and better PFS (4.8 vs 1.8 months, HR 0.48 (95% CI 0.26 to 0.90), p=0.019) to ICI mono-treatment than other IPs (figure 5A), while there was no significant difference in the PD-L1 expression level (online supplemental figure S3 and online supplemental figure S4). In the ATLLAS cohort, no significant differences were observed between the ABCP and PC groups based on inflamed IP or non-inflamed IP (p=0.190; online supplemental figure S5).

We further evaluated the potential roles of TILs in CA, ECs in CA, fibers in CA plus CS, and the TLS area per CA.

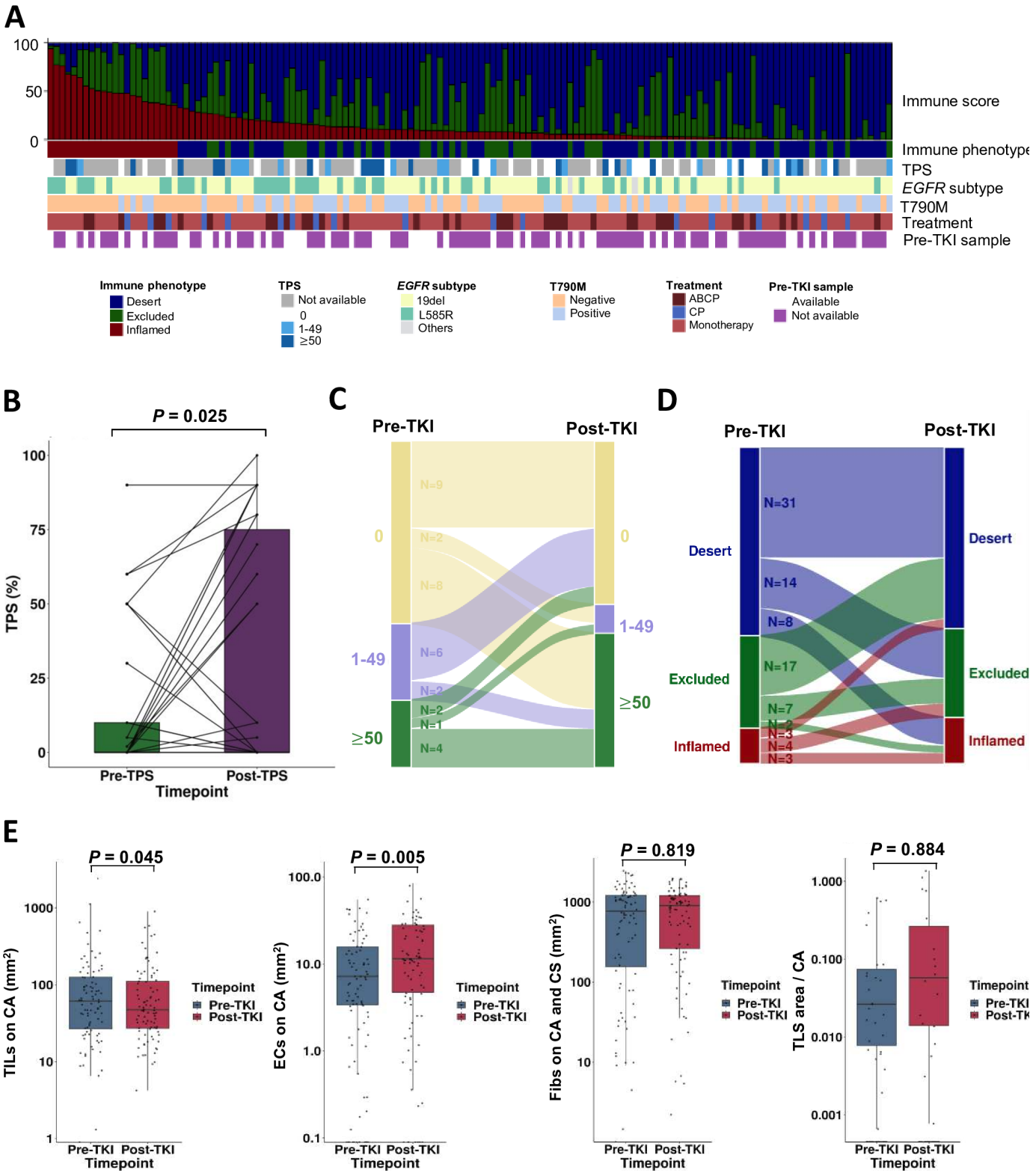

Figure 3 Dynamic change of TME after acquired resistance to EGFR-TKI. (A) Overall landscape assessed by AI-IP analysis. (B) Dynamic change of PD-L1 expression after resistance to EGFR-TKI. (C) Alluvial plot presenting the change of PD-L1 expression after resistance to EGFR TKI. (D) Alluvial plot presenting the change of AI-IPs comparing pre-EGFR-TKI and post-EGFR-TKI treatment samples. (E) Dynamic change of AI-powered TME analysis in patients after resistance to EGFR-TKI. ABCP, atezolizumab plus bevacizumab, paclitaxel, and carboplatin; AI, artificial intelligence; CA, cancer area; CP, carboplatin plus paclitaxel; CS, cancer stroma; EC, endothelial cell; EGFR, epidermal growth factor receptor; Fibs, fibroblasts; TIL, tumor-infiltrating lymphocyte; TKI, tyrosine kinase inhibitor; TLS, tertiary lymphoid structure; TPS, tumor proportion score.

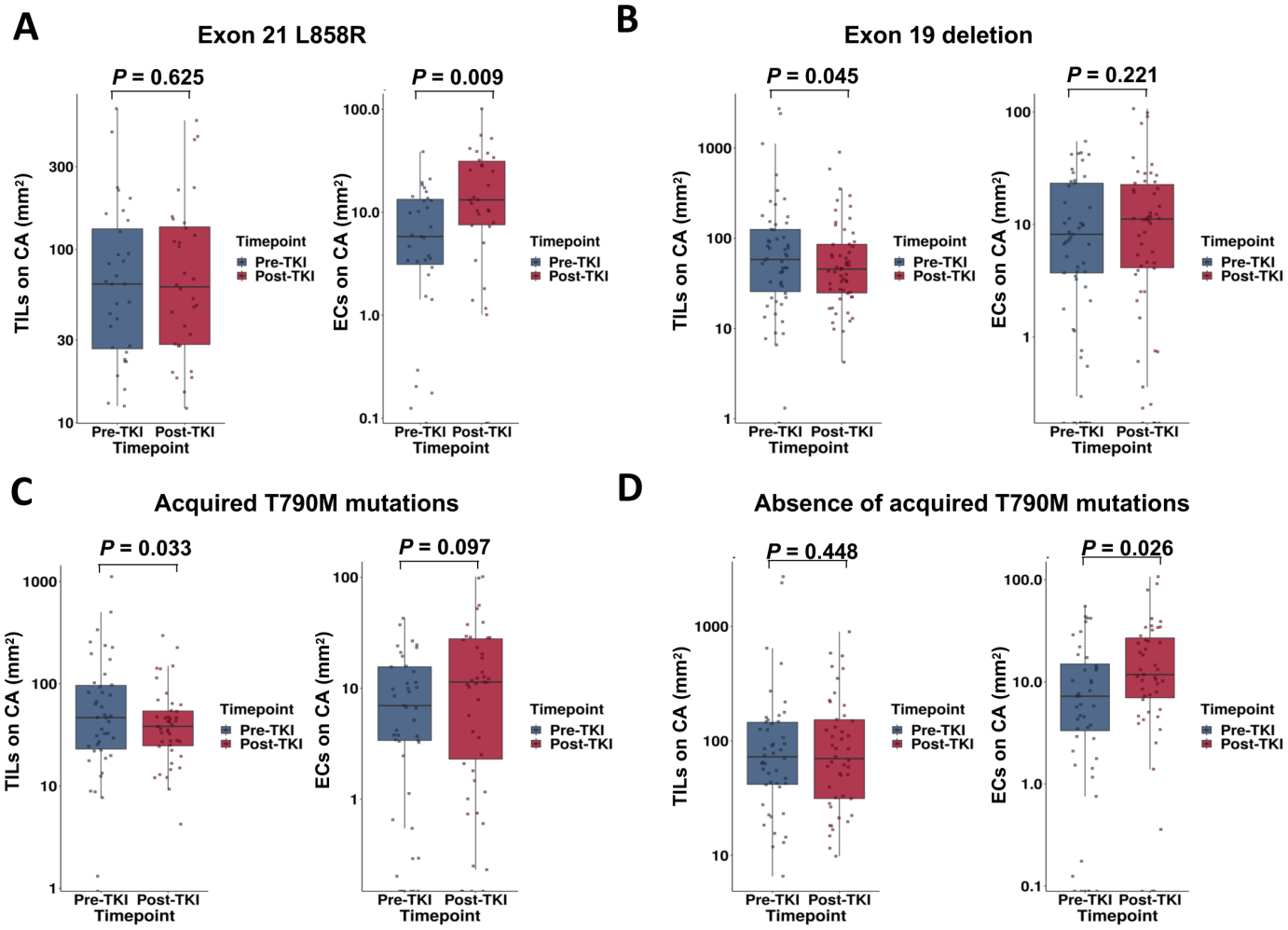

Figure 4 Dynamic change of TME according to the EGFR mutant type. Comparison analysis of pre-TKI and post-TKI TILs on CA and ECs on CA based on exon 21 L858R (A), exon 19 deletion (B), acquired T790M-positive (C), and acquired T790M-negative (D) status. P values were calculated using the Wilcoxon rank-sum test. CA, cancer area; EC, endothelial cell; EGFR, epidermal growth factor receptor; TIL, tumor-infiltrating lymphocytes.

Interestingly, among the patients treated with ICIs monotherapy, patients with higher TILs in CA demonstrated superior overall response rate (ORR, 41.7% vs 9.7%, p=0.003) and PFS (4.9 vs 1.8 months, HR 0.41 (95% CI 0.21 to 0.79), p=0.006; figure 5B,C). Similarly, higher EC levels in CA correlated with better ORR (19.3% vs 3.7%, p<0.01) and PFS (2.0 vs 1.4 months, HR 0.44 (95% CI 0.28 to 0.71), p<0.001; figure 5B,C). In contrast, patients with higher Fibs in CA and CS exhibited inferior PFS (1.8 vs 2.0 months, HR 1.68 (95% CI 1.05 to 2.68), p=0.026; figure 5C). Similar trends were observed in the multivariable analysis (online supplemental table 4). In the ATTLAS trial cohort, these factors were associated with clinical benefits from ABCP, with a significant association for TILs (HR 0.42 (95% CI 0.19 to 0.91, p=0.027)) and a marginal association for ECs (HR 0.29 (95% CI 0.07 to 1.15, p=0.067); figure 5D,E and online supplemental figure S5).

DISCUSSION

In this study, we used an AI-powered TME analyzer to evaluate dynamic changes in the TME following acquired resistance to EGFR-TKIs in patients with NSCLC. Notably, the AI-derived analyses of TILs, Fibs, ECs, and TLSs demonstrated strong correlations with the results obtained from spatial and bulk transcriptomics, underscoring the robustness of the AI-powered approach. Our findings revealed significant reductions in TILs and increases in ECs within the CA following EGFR-TKI treatment. These changes were closely associated with clinical outcomes, as higher TILs or EC levels in the CA were significantly associated with improved response rates and prolonged PFS in patients receiving ICI monotherapy or combination therapy.

We previously reported that AI-IP analysis based on spatial TIL distribution[22–24] could effectively stratify IPs to predict the efficacy of ICIs. Similarly, in the present study, patients exhibiting inflamed IPs (4.8 vs 1.8 months, p=0.019) or higher TILs on CA (4.9 vs 1.8 months, p=0.006) after EGFR-TKI treatment exhibited significantly better PFS than those with other IPs. Notably, changes in IPs were observed following resistance to TKI, suggesting that EGFR-TKIs could induce TME remodeling, highlighting the need for post-TKI biopsy to guide treatment strategies.

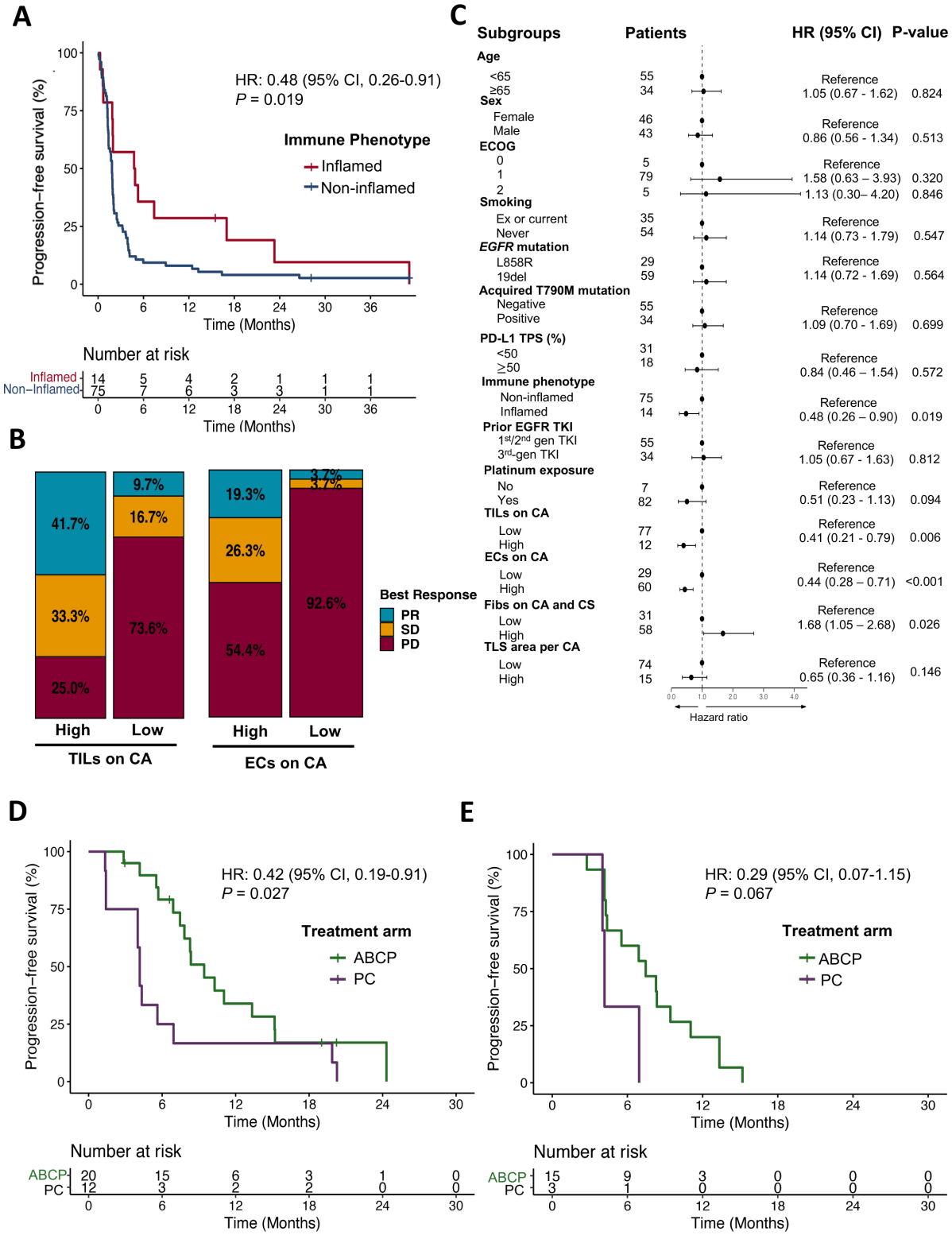

Figure 5 Efficacy outcomes with ICI after acquired resistance to EGFR-TKI. (A) Progression-free survival with ICIs monotherapy according to the IP after acquired resistance to EGFR-TKI. (B) Proportion bar plot indicating best response according to the TILs on CA, and ECs on CA. (C) Forest plot of HR (dot) and 95% CI (arrow) for PFS and OS according to the baseline characteristics and variables inferred from AI-powered TME analyzer. (D–E) Progression-free survival comparison between the ABCP arm and the PC arm in patients with higher TILs on CA (D) or ECs on CA (E) following EGFR-TKI treatment in the ATTLAS cohort. ABCP, atezolizumab plus bevacizumab, paclitaxel, and carboplatin; CA, cancer area; CS, cancer stroma; EC, endothelial cell; ECOG, Eastern Cooperative Oncology Group; EGFR, epidermal growth factor receptor; Fibs, fibroblasts; ICI, immune-checkpoint inhibitor; IP, immune-phenotype; PC, pemetrexed plus carboplatin; PD, progressive disease; PD-L1, programmed death-ligand 1; PR, partial response; SD, stable disease; TIL, tumor-infiltrating lymphocyte; TKI, tyrosine kinase inhibitor; TLS, tertiary lymphoid structure; TPS, tumor proportion score.

Interestingly, the observed TME changes following EGFR-TKI resistance varied according to the mutation subtype. Patients with 19del or acquired T790M mutations exhibited a reduction in TILs, transitioning toward an immune-desert phenotype, likely reflecting TME remodeling in response to EGFR signaling inhibition. Although EGFR-driven pathways (such as PI3K/AKT and MAPK/ERK) are suppressed by TKI therapy, compensatory mechanisms, such as upregulation of immunosuppressive signals (such as PD-L1 and transforming growth factor-β) or alterations in angiogenic pathways (such as VEGF), may drive immune cell exclusion of these subtypes.[46] Conversely, patients with L858R mutations had preserved TIL levels and demonstrated increased EC abundance, possibly because of the differential modulation of vascular remodeling or immune signaling pathways post-TKI.[47] These distinct TME adaptations may explain the superior response to ICI-based therapies observed in patients with L858R mutations, as supported by the ATTLAS trial,[15] where patients with L858R mutations showed favorable outcomes in the ABCP group. Collectively, these findings suggest that mutation-specific TME characteristics contribute to the differential clinical benefits observed across *EGFR* mutation subtypes and warrant further investigation.

Our study revealed an increase in the proportion of patients with PD-L1 TPS ≥50% post-EGFR-TKI treatment, consistent with prior reports.[14] This increase may reflect treatment-induced changes in the TME, such as enhanced PD-L1 expression via compensatory mechanisms following the inhibition of EGFR signaling. However, unlike previous reports where high PD-L1 levels were associated with improved outcomes,[14] our cohort showed no clear predictive value of PD-L1 TPS ≥0%. This may be explained by the presence of immunosuppressive factors in EGFR-mutated NSCLC, such as increased regulatory T-cell activity and CD73 expression, which may limit immune activation despite high PD-L1 levels.[14] These findings underscore the challenges of relying on static biomarkers such as PD-L1 TPS to capture the dynamic and multifaceted nature of the TME, highlighting the potential of AI-powered TME analysis to provide additional insights into TME characteristics.

While our study focused on H&E-based AI analysis of the TME, several recent studies have also employed AI-powered analysis to characterize tumor-intrinsic pathological patterns, demonstrating clinical relevance.[48 49] Furthermore, as spatial omics technologies, including spatial transcriptomics, spatial proteomics, and multiplexed imaging, continue to evolve, they are increasingly being integrated into clinical research to enable more comprehensive dissection of the TME.[50–54] Combining such approaches with spatial molecular data may enhance the precision of immune landscape profiling and facilitate the identification of more robust and clinically actionable biomarkers.[55 56]

This study has several limitations. First, the relatively small cohort with limited paired pretreatment data limits the generalizability of our findings. Second, heterogeneity in *EGFR* mutation subtypes, timing of post-TKI biopsies, biopsy site or specimen type, and subsequent treatment patterns may have affected the assessment of TME dynamics, although these reflect real-world clinical practice. Third, the safety profile of ICIs could not be comprehensively assessed due to the retrospective design. Fourth, while exploratory biomarkers such as TLS, Fibs, and ECs were associated with clinical outcomes, their interpretation relied on cohort-specific cutoffs that may not fully capture underlying biological heterogeneity and could limit generalizability. Future studies involving larger, multi-institutional cohorts are required to validate these findings and establish clinically applicable thresholds. Fifth, functional immune states such as T-cell exhaustion could not be assessed from H&E images; expanding spatial transcriptomic and proteomic datasets may enable the development of more refined AI models for comprehensive TME characterization.

In conclusion, AI-powered TME analysis provides a robust framework for evaluating TME changes and stratifying patients with NSCLC according to ICI efficacy after developing EGFR-TKI resistance. Higher TILs or ECs in the CA were significantly associated with a favorable response to ICI or combination treatment with ICI as a subsequent treatment.

Author affiliations
[1]Division of Hematology-Oncology, Department of Medicine, Samsung Medical Center, Sungkyunkwan University School of Medicine, Seoul, Republic of Korea
[2]Department of Digital Health, SAIHST, Sungkyunkwan University, Seoul, Republic of Korea
[3]Department of Oncology, Asan Medical Center, University of Ulsan College of Medicine, Seoul, Republic of Korea
[4]Department of Health Sciences and Technology, SAIHST, Sungkyunkwan University, Seoul, Republic of Korea
[5]Lunit Inc, Seoul, Republic of Korea
[6]Department of Pathology and Translational Genomics, Samsung Medical Center, Sungkyunkwan University School of Medicine, Seoul, Republic of Korea
[7]Department of Clinical Research and Evaluation, Samsung Advanced Institute of Health Sciences and Technology, Sungkyunkwan University, Seoul, Republic of Korea

Contributors YHB and G-HP: conception and design of the study, planning, data curation, formal analysis, investigation, visualization, methodology, drafting of the original manuscript, and critical review and editing. JWO: formal analysis, visualization, methodology, drafting of the original manuscript, and critical review and editing. J-GJ: investigation, methodology, and critical review and editing. BL, CYJ, HK, JK, SP, HAJ, J-MS, JSA, M-JA, and Y-LC: resources and critical review and editing. SH, CHA, SA, and C-YO: conception, resources, and critical review and editing. S-HL: conception and design of the study, planning, resources, formal analysis, investigation, methodology, supervision, and critical review and editing, and served as the guarantor of the study, having full access to all the data and taking full responsibility for the integrity of the work and the decision to submit for publication.

Funding This research was supported by the Bio&Medical Technology Development Program of the National Research Foundation (NRF) funded by the Korean government (MSIT) (grant number: RS-2023-00225255). This work was supported by the NRF grant funded by the Korea government (MSIT) (grant number: RS-2025-00519956). This research was supported by a grant of the Korea Health Technology R&D Project through the Korea Health Industry Development Institute (KHIDI), funded by the Ministry of Health & Welfare, Republic of Korea (grant number: RS-2020-KH088685). This work was supported by the Future Medicine

2030 Project of the Samsung Medical Center (#SMX1250111, #SMO1250061). This research was supported by a grant of the Korea-US Collaborative Research Fund (KUCRF), funded by the Ministry of Science and ICT and Ministry of Health & Welfare, Republic of Korea (grant number: RS-2024-00466776). This research was supported by a grant of Korean ARPA-H Project through the Korea Health Industry Development Institute (KHIDI), funded by the Ministry of Health & Welfare, Republic of Korea (grant number: RS-2024-00512539).

Competing interests Nothing directly related to this work. Outside of this work, SH reports employment at Lunit. HAJ reported advisory roles with Yuhan, Guardant, and AIMEDBIO, and received research funding from Yuhan. JSA received honoraria from Pfizer, Roche, BC World Pharmaceutical, Yuhan, Hanmi, Novartis, JW Pharmaceutical, Amgen, Boehringer Ingelheim, Menarini, Kyowa Kirin, AstraZeneca, Bayer, Lilly, Takeda, Boryung, and Samyang; and held advisory roles with Bayer, Yooyoung Pharmaceutical, Pharmbio Korea, Guardant Health, Yuhan, ImmuneOncia, Therapex, Daiichi Sankyo Korea, and Roche. M-JA received honoraria from AstraZeneca, Lilly, MSD, Takeda, Amgen, Merck Serono, and Yuhan; held advisory roles with AstraZeneca, Lilly, MSD, Takeda, Alpha Pharmaceutical, Amgen, Merck Serono, Pfizer, Yuhan, and Arcus Ventures; and received research funding from Yuhan. S-HL received honoraria from AstraZeneca/MedImmune, Roche, Merck Sharp & Dohme, Eli Lilly, Amgen, Abion, Daiichi Sankyo, and Yuhan; held consulting or advisory roles with AstraZeneca, Roche, Merck Sharp & Dohme, Pfizer, Eli Lilly, BMS/Ono, Daiichi Sankyo, Takeda, Janssen, IMBdx, Abion, Beigene, and ImmuneOncia; received research funding from Merck Sharp & Dohme, AstraZeneca, and Lunit; and received travel, accommodations, and expenses from Novartis. JWO, SH, CHA, SA, and C-YO are employees of Lunit.

Patient consent for publication Not applicable.

Ethics approval This study was approved by the Institutional Review Board (IRB) of Samsung Medical Center (IRB approval numbers: 2013-10-112, 2018-06-163, and 2018-04-048). Informed consent was waived due to the retrospective nature of the analysis in the overall patient cohort. However, for patients who underwent bulk RNA sequencing, written informed consent was obtained prior to tissue collection and analysis. Additionally, in the subcohort enrolled in the ATTLAS trial, clinical data were prospectively collected, and written informed consent was obtained from all participants (IRB approval number: 2019-03-027). This study was conducted in accordance with the Declaration of Helsinki.

Provenance and peer review Not commissioned; externally peer reviewed.

Data availability statement Data are available on reasonable request. All requests for raw and analyzed data and materials should be directed to S-HL and will be promptly reviewed by Samsung Medical Center to determine whether the request is subject to any intellectual property or confidentiality obligations. Patient-related data not included in this article were generated as part of a clinical trial and may be subject to patient confidentiality restrictions. Any data and materials that can be shared will be provided under a material transfer agreement. All analyses were performed using publicly available software, as described in the 'Materials and methods' section.

ORCID iDs
Yeong Hak Bang https://orcid.org/0000-0001-6544-6431
Jin Woo Oh https://orcid.org/0000-0002-3545-5481
Sehhoon Park https://orcid.org/0000-0001-9467-461X
Jong-Mu Sun https://orcid.org/0000-0001-9683-4111

REFERENCES

1 Hsu W-H, Yang JC-H, Mok TS, *et al*. Overview of current systemic management of EGFR-mutant NSCLC. *Ann Oncol* 2018;29:i3–9.
2 Ramalingam SS, Vansteenkiste J, Planchard D, *et al*. Overall Survival with Osimertinib in Untreated, *EGFR*-Mutated Advanced NSCLC. *N Engl J Med* 2020;382:41–50.
3 Cho BC, Ahn M-J, Kang JH, *et al*. Lazertinib Versus Gefitinib as First-Line Treatment in Patients With *EGFR*-Mutated Advanced Non-Small-Cell Lung Cancer: Results From LASER301. *J Clin Oncol* 2023;41:4208–17.
4 Cho BC, Lu S, Felip E, *et al*. Amivantamab plus Lazertinib in Previously Untreated *EGFR*-Mutated Advanced NSCLC. *N Engl J Med* 2024;391:1486–98.
5 Planchard D, Jänne PA, Cheng Y, *et al*. Osimertinib with or without Chemotherapy in *EGFR*-Mutated Advanced NSCLC. *N Engl J Med* 2023;389:1935–48.
6 Zhou F, Guo H, Xia Y, *et al*. The changing treatment landscape of EGFR-mutant non-small-cell lung cancer. *Nat Rev Clin Oncol* 2025;22:95–116.
7 Hendriks LE, Kerr KM, Menis J, *et al*. Non-oncogene-addicted metastatic non-small-cell lung cancer: ESMO Clinical Practice Guideline for diagnosis, treatment and follow-up. *Ann Oncol* 2023;34:358–76.
8 Reck M, Rodríguez-Abreu D, Robinson AG, *et al*. Pembrolizumab versus Chemotherapy for PD-L1-Positive Non-Small-Cell Lung Cancer. *N Engl J Med* 2016;375:1823–33.
9 Mok TSK, Wu Y-L, Kudaba I, *et al*. Pembrolizumab versus chemotherapy for previously untreated, PD-L1-expressing, locally advanced or metastatic non-small-cell lung cancer (KEYNOTE-042): a randomised, open-label, controlled, phase 3 trial. *Lancet* 2019;393:1819–30.
10 Lee CK, Man J, Lord S, *et al*. Checkpoint Inhibitors in Metastatic EGFR-Mutated Non-Small Cell Lung Cancer-A Meta-Analysis. *J Thorac Oncol* 2017;12:403–7.
11 Gainor JF, Shaw AT, Sequist LV, *et al*. *EGFR* Mutations and *ALK* Rearrangements Are Associated with Low Response Rates to PD-1 Pathway Blockade in Non–Small Cell Lung Cancer: A Retrospective Analysis . *Clin Cancer Res* 2016;22:4585–93.
12 Mok TSK, Nakagawa K, Park K, *et al*. LBA8 Nivolumab (NIVO) + chemotherapy (chemo) vs chemo in patients (pts) with EGFR-mutated metastatic non-small cell lung cancer (mNSCLC) with disease progression after EGFR tyrosine kinase inhibitors (TKIs) in CheckMate 722. *Ann Oncol* 2022;33:S1561–2.
13 Yang JC-H, Lee DH, Lee J-S, *et al*. Phase III KEYNOTE-789 Study of Pemetrexed and Platinum With or Without Pembrolizumab for Tyrosine Kinase Inhibitor–Resistant, *EGFR*-Mutant, Metastatic Nonsquamous Non-Small Cell Lung Cancer. *J Clin Oncol* 2024;42:4029–39.
14 Isomoto K, Haratani K, Hayashi H, *et al*. Impact of EGFR-TKI Treatment on the Tumor Immune Microenvironment in *EGFR* Mutation-Positive Non-Small Cell Lung Cancer. *Clin Cancer Res* 2020;26:2037–46.
15 Park S, Kim TM, Han J, *et al*. Phase III, Randomized Study of Atezolizumab Plus Bevacizumab and Chemotherapy in Patients With EGFR- or ALK-Rearranged or Translocated Non-Small-Cell Lung Cancer (ATTLAS, KCSG-LU19-04). *J Clin Oncol* 2024;42:1241–51.
16 Bagaev A, Kotlov N, Nomie K, *et al*. Conserved pan-cancer microenvironment subtypes predict response to immunotherapy. *Cancer Cell* 2021;39:845–65.
17 Cho J-W, Park S, Kim G, *et al*. Dysregulation of TFH-B-TRM lymphocyte cooperation is associated with unfavorable anti-PD-1 responses in EGFR-mutant lung cancer. *Nat Commun* 2021;12:6068.
18 Park S, Cha H, Kim HS, *et al*. Transcriptional upregulation of CXCL13 is correlated with a favorable response to immune checkpoint inhibitors in lung adenocarcinoma . *Cancer Med* 2023;12:7639–50.
19 Kang J, Lee JH, Cha H, *et al*. Systematic dissection of tumor-normal single-cell ecosystems across a thousand tumors of 30 cancer types. *Nat Commun* 2024;15:4067.
20 Khoury T, Peng X, Yan L, *et al*. Tumor-Infiltrating Lymphocytes in Breast Cancer: Evaluating Interobserver Variability, Heterogeneity, and Fidelity of Scoring Core Biopsies. *Am J Clin Pathol* 2018;150:441–50.
21 Van Bockstal MR, François A, Altinay S, *et al*. Interobserver variability in the assessment of stromal tumor-infiltrating lymphocytes (sTILs) in triple-negative invasive breast carcinoma influences the association with pathological complete response: the IVITA study. *Mod Pathol* 2021;34:2130–40.
22 Park S, Ock C-Y, Kim H, *et al*. Artificial Intelligence-Powered Spatial Analysis of Tumor-Infiltrating Lymphocytes as Complementary Biomarker for Immune Checkpoint Inhibition in Non-Small-Cell Lung Cancer. *J Clin Oncol* 2022;40:1916–28.

23 Shen J, Choi Y-L, Lee T, *et al*. Inflamed immune phenotype predicts favorable clinical outcomes of immune checkpoint inhibitor therapy across multiple cancer types. *J Immunother Cancer* 2024;12:e008339.
24 Bang YH, Lee C, Bang K, *et al*. Artificial Intelligence-Powered Spatial Analysis of Tumor-Infiltrating Lymphocytes as a Potential Biomarker for Immune Checkpoint Inhibitors in Patients with Biliary Tract Cancer. *Clin Cancer Res* 2024;30:4635–43.
25 Chen Z, Wang X, Jin Z, *et al*. Deep learning on tertiary lymphoid structures in hematoxylin-eosin predicts cancer prognosis and immunotherapy response. *NPJ Precis Oncol* 2024;8:73.
26 Rigamonti A, Viatore M, Polidori R, *et al*. Integrating AI-Powered Digital Pathology and Imaging Mass Cytometry Identifies Key Classifiers of Tumor Cells, Stroma, and Immune Cells in Non-Small Cell Lung Cancer. *Cancer Res* 2024;84:1165–77.
27 Jung M, Kim JY, Kang M, *et al*. Abstract 276: Artificial intelligence-powered analysis of tumor-stroma ratio and fibroblast density as prognostic indicators in colorectal cancer. *Cancer Res* 2024;84:276.
28 Hwang J-E, Kim S-S, Bang H-J, *et al*. Tumor Immune Microenvironment Biomarkers for Recurrence Prediction in Locally Advanced Rectal Cancer Patients after Neoadjuvant Chemoradiotherapy. *Cancers (Basel)* 2024;16.
29 Ryu K, Hwang S, Park J. Proceedings of the IEEE/CVF Conference on Computer Vision and Pattern Recognition; 2023
30 Janesick A, Shelansky R, Gottscho AD, *et al*. High resolution mapping of the tumor microenvironment using integrated single-cell, spatial and in situ analysis. *Nat Commun* 2023;14:8353.
31 Dunham I, Kundaje A, Aldred SF. An integrated encyclopedia of DNA elements in the human genome. *Nature New Biol* 2012;489:57–74.
32 Ritchie ME, Phipson B, Wu D, *et al*. limma powers differential expression analyses for RNA-sequencing and microarray studies. *Nucleic Acids Res* 2015;43:e47–e.
33 Hänzelmann S, Castelo R, Guinney J. GSVA: gene set variation analysis for microarray and RNA-seq data. *BMC Bioinformatics* 2013;14:7.
34 Liberzon A, Birger C, Thorvaldsdóttir H, *et al*. The Molecular Signatures Database (MSigDB) hallmark gene set collection. *Cell Syst* 2015;1:417–25.
35 Ayers M, Lunceford J, Nebozhyn M, *et al*. IFN-γ-related mRNA profile predicts clinical response to PD-1 blockade. *J Clin Invest* 2017;127:2930–40.
36 Rooney MS, Shukla SA, Wu CJ, *et al*. Molecular and genetic properties of tumors associated with local immune cytolytic activity. *Cell* 2015;160:48–61.
37 Galon J, Angell HK, Bedognetti D, *et al*. The Continuum of Cancer Immunosurveillance: Prognostic, Predictive, and Mechanistic Signatures. *Immunity* 2013;39:11–26.
38 Thorsson V, Gibbs DL, Brown SD, *et al*. The Immune Landscape of Cancer. *Immunity* 2018;48:812–30.
39 Cabrita R, Lauss M, Sanna A, *et al*. Tertiary lymphoid structures improve immunotherapy and survival in melanoma. *Nature New Biol* 2020;577:561–5.
40 Meylan M, Petitprez F, Becht E, *et al*. Tertiary lymphoid structures generate and propagate anti-tumor antibody-producing plasma cells in renal cell cancer. *Immunity* 2022;55:527–41.
41 Lausen B, Schumacher M. Maximally Selected Rank Statistics. *Biometrics* 1992;48:73.
42 Starke RD, Ferraro F, Paschalaki KE, *et al*. Endothelial von Willebrand factor regulates angiogenesis. *Blood* 2011;117:1071–80.
43 Privratsky JR, Newman PJ. PECAM-1: regulator of endothelial junctional integrity. *Cell Tissue Res* 2014;355:607–19.
44 Nurmik M, Ullmann P, Rodriguez F, *et al*. In search of definitions: Cancer-associated fibroblasts and their markers. *Int J Cancer* 2020;146:895–905.
45 Okuno K, Ikemura K, Okamoto R, *et al*. CAF-associated genes putatively representing distinct prognosis by in silico landscape of stromal components of colon cancer. *PLoS One* 2024;19:e0299827.
46 Peng S, Wang R, Zhang X, *et al*. EGFR-TKI resistance promotes immune escape in lung cancer via increased PD-L1 expression. *Mol Cancer* 2019;18:165.
47 Chen S, Tang J, Liu F, *et al*. Changes of tumor microenvironment in non-small cell lung cancer after TKI treatments. *Front Immunol* 2023;14:1094764.
48 Pan X, AbdulJabbar K, Coelho-Lima J, *et al*. The artificial intelligence-based model ANORAK improves histopathological grading of lung adenocarcinoma. *Nat Cancer* 2024;5:347–63.
49 Zhao Y, He S, Zhao D, *et al*. Deep learning-based diagnosis of histopathological patterns for invasive non-mucinous lung adenocarcinoma using semantic segmentation. *BMJ Open* 2023;13:e069181.
50 Williams CG, Lee HJ, Asatsuma T, *et al*. An introduction to spatial transcriptomics for biomedical research. *Genome Med* 2022;14:68.
51 Sozanska AM, Pescia C, Thomas E, *et al*. Entering the era of spatial transcriptomics: opportunities and challenges for pathology. *Diagn Histopathol (Oxf)* 2025;31:257–66.
52 Tagore S, Caprio L, Amin AD, *et al*. Single-cell and spatial genomic landscape of non-small cell lung cancer brain metastases. *Nat Med* 2025;31:1351–63.
53 Shi Q, Chen Y, Li Y, *et al*. Cross-tissue multicellular coordination and its rewiring in cancer. *Nature New Biol* 2025;643:529–38.
54 Sorin M, Rezanejad M, Karimi E, *et al*. Single-cell spatial landscapes of the lung tumour immune microenvironment. *Nature New Biol* 2023;614:548–54.
55 Chelebian E, Avenel C, Wählby C. Combining spatial transcriptomics with tissue morphology. *Nat Commun* 2025;16:4452.
56 Li Y, Stanojevic S, Garmire LX. Emerging artificial intelligence applications in Spatial Transcriptomics analysis. *Comput Struct Biotechnol J* 2022;20:2895–908.